Small-Signal Modeling of Dissipative Carrier Transport in Nanodevices with Nonequilibrium Green's Functions

Alberto Tibaldi,[1,2,*] Michele Goano,[1,2] and Francesco Bertazzi[1,2]

[1] *DET, Politecnico di Torino, Torino, Italy*

[2] *IEIIT-CNR, Torino, Italy*

(Received 8 March 2023; revised 9 May 2023; accepted 10 May 2023; published 6 June 2023)

Emerging applications in the field of finite-frequency mesoscopic physics require accurate modeling tools for the evaluation of carrier-transport dynamics, modulation bandwidth, and frequency conversion effects in nanodevices. With foundations in advanced concepts of many-body and quantum field theories, the nonequilibrium Green's function technique is widely adopted in the calculation of steady-state carrier-transport properties of nanostrucures, while the evaluation of the frequency response is so far largely unexplored by genuine quantum models. Guided by the connection with drift-diffusion solvers within a local description of carrier-phonon scattering, we propose an accurate, yet computationally efficient nonequilibrium Green's function model of dissipative carrier transport to study the small-signal properties of semiconductor nanostructures. From the numerical evaluation of steady-state Green's functions and their functional derivatives, we compute spectrally resolved observables expressed in terms of familiar microscopic quantities germane to the drift-diffusion framework, the most prevalent tool in semiclassical device simulation. Besides drastically improving the convergence properties, the exact Jacobian, complemented with the contribution of the displacement current, gives access to the small-signal admittance. Current-conserving boundary conditions suitable for small-signal analysis provide the correct physical behavior near the contacts. Numerical examples show the accuracy and flexibility of the proposed model.

DOI: 10.1103/PhysRevApplied.19.064020

I. INTRODUCTION

Modeling the frequency response of quantum systems is essential to design nanostructured materials for future high-speed (opto)electronic applications. While most theoretical and experimental studies of quantum transport in semiconductor nanostructures have been focused on static electrical characteristics, emerging applications require physical insight in the high-frequency dynamical properties. For example, type-II superlattice (T2SL) photodetectors are usually designed to optimize steady-state figures of merit, such as quantum efficiency and detectivity, but recent innovations in the areas of free-space optical communication and frequency-comb spectroscopy impose additional requirements in terms of bandwidth [1,2]. A similar argument can be made for GaN-based visible LEDs, whose popularity in solid-state lighting applications has laid the foundation for their application as light sources for high-speed visible light communication, a cutting-edge alternative to traditional wireless systems [3].

Encompassing different transport regimes such as miniband propagation, sequential tunneling and Wannier-Stark hopping [4,5], the sophisticated physics of carrier transport in T2SL photodetectors calls for a rigorous treatment of quantum effects in the calculation of steady-state and small-signal characteristics. Perhaps, the most representative evidence of the limitations of (quantum corrected) drift-diffusion models is a long-standing discussion concerning the loss mechanisms in visible LEDs, which has been living by the antinomies of "droop theories," diverse and often antithetic explanations for the decline of the internal quantum efficiency at high current densities [6,7]. Among genuine quantum approaches, the nonequilibrium Green's function (NEGF) formalism is the most versatile and powerful. With foundations in advanced concepts of many-body and quantum field theories, NEGF has found wide-spread application in the modeling of advanced (opto)electronic nanodevices [8–10]. NEGF approaches are generally considered more suited to steady-state carrier transport rather than transient and frequency responses, since, in the presence of time-dependent fields, the translational time invariance is broken, and the resulting complex two-times dependence of the Green's functions increases the complexity of the problem compared to more common methods, such as density matrix and Wigner-function techniques [11,12].

Recent advances enabled by the generalized Kadanoff-Baym ansatz [13] have significantly increased

*alberto.tibaldi@polito.it

the time scales accessible to time-domain NEGF simulations, but computational requirements imposed by numerical stability constraints and "memory effects," i.e., the functional dependence on the full history of Green's functions, still make time propagation impractical at gigahertz frequencies.

Frequency-domain analysis seems more appropriate to capture the response of quantum nanodevices at subterahertz frequencies, but the development of ac NEGF models has been hampered by difficulties arising from the two-times structure of the NEGF formalism. Switching from time coordinates to the energy representation requires a double-time Fourier transform [14], as the ac field generates sidebands in Green's functions at integer multiples of the driving frequency, leading to surprising effects in semiconductor superlattices, such as photon-assisted tunneling, dynamical localization (miniband collapse by radiation), and absolute negative conductance (i.e., negative current for positive bias) [4,15]. Following Ref. [16], a Floquet-Green's function approach for periodic Hamiltonians was developed to study frequency-conversion effects induced by the lasing field in quantum cascade lasers [17,18]. If the linear response to small-signal modulations is sought, the computational effort can be eased, as higher-order terms of the Floquet series can be neglected [19–22].

Another difficulty in the development of ac NEGF models is the treatment of the displacement current. Current partition schemes were initially proposed to ensure the conservation of the total current (particle plus displacement) and gauge invariance, i.e., the currents of a multiprobe system should not change if all bias voltages are shifted by a constant amount [23]. Later studies showed that both conditions are verified when long-range Coulomb interactions are included on the Hartree level by means of the self-consistent solution of the Poisson equation [24,25]. A current-conserving NEGF theory of ac quantum transport based on the full dynamic solution of Maxwell's equations was presented in Ref. [26] to study radiated fields and crosstalk in high-frequency circuits.

Recently, we proposed a NEGF approach based on the Büttiker-probe formalism to provide a simplified description of dissipative carrier transport in nanodevices, with intraband scattering (carrier-phonon interactions) modeled with local self-energies, and interband transitions (radiative and nonradiative recombination processes) included by means of generation-recombination rates [27]. A Newton-Raphson scheme based on the numerical evaluation of functional derivatives drastically improves the convergence of steady-state calculations, but also provides the foundation for the small-signal analysis. In this work, guided by the connection with drift-diffusion (DD) models, we linearize the dissipative NEGF model presented in Ref. [27] to compute the frequency response of semiconductor nanostructures. We address the problem of charge imbalance near the contacts by developing boundary conditions (BCs) suitable for small-signal analysis, ensuring that the current flux at contact-device boundaries is divergenceless. For brevity, we present the model for unipolar carrier transport, but the extension to the bipolar case is straightforward. With numerical simulations of a resistive *n-i-n* structure and a resonant tunneling diode (RTD), we show that the proposed NEGF model provides a rigorous and intuitive description of quantum transport in steady-state and small-signal conditions, by means of spectrally resolved single-particle properties (local density of states and spectral currents) expressed in terms of microscopic quantities (quasi-Fermi-levels and electrostatic potential) commonly used in semiclassical device simulations.

II. THEORY

The quantum kinetic version of the drift-diffusion model reads [28]

$$\nabla \cdot [\varepsilon(r_1)\nabla\phi(1)] = e[n(1) - N_D(r_1)] \quad (1a)$$

$$\frac{\partial n(1)}{\partial t_1} - \frac{1}{e}\nabla \cdot J_n(1) + U_n(1) = 0, \quad (1b)$$

with $1 \equiv (r_1, t_1)$ and

$$n(1) = -i\hbar\, G^<(1,1) \quad (2a)$$

$$\nabla \cdot J_n(1) = -e \lim_{1'\to 1}[H(r_1) - H(r_{1'})]G^<(1,1') \quad (2b)$$

$$U_n(1) = \int d2 \left[\Sigma^R(1,2)G^<(2,1) + \Sigma^<(1,2)G^A(2,1) - G^R(1,2)\Sigma^<(2,1) - G^<(1,2)\Sigma^A(2,1)\right], \quad (2c)$$

where e is the electron charge, ϕ is the (Hartree) electrostatic potential, n is the electron density, J_n is the (particle) current density, N_D is the donor doping density, ε is the dielectric constant, H is the Hamiltonian of the noninteracting system, and G^γ are the Keldysh components of Green's function ($\gamma = <, >, R, A$). The self-energy Σ encodes intraband scattering processes (interactions with phonons), interband transitions (radiative and nonradiative recombination processes), and the coupling to the contacts. Similar expressions exist for holes in terms of the greater Green's function $G^>$. Assuming a single-band effective-mass Hamiltonian for one-dimensional layered systems

$$H(k,z) = -\frac{\partial}{\partial z}\frac{\hbar^2}{2m_n^*}\frac{\partial}{\partial z} - e\phi(z) + \Delta E_C(z) + \frac{\hbar^2 k^2}{2m_n^*}, \quad (3)$$

where z is the symmetry-broken coordinate, k is the norm of the in-plane wave vector, m_n^* is electron effective mass,

and ΔE_C is the conduction-band offset (nonzero only in heterostructures), we find in steady-state conditions

$$\frac{\partial}{\partial z}\left[\varepsilon(z)\frac{\partial}{\partial z}\phi(z)\right] = e[n(z) - N_D(z)] \tag{4a}$$

$$-\frac{1}{e}\frac{\partial}{\partial z}J_n(z) + U_n(z) = 0 \tag{4b}$$

with

$$n(z) = -i\sigma \int \frac{dE}{2\pi} G^<(z,z,E) \tag{5a}$$

$$\frac{\partial}{\partial z}J_n(z) = -\sigma e \lim_{z'\to z} \int \frac{dE}{2\pi\hbar}[H(z) - H(z')]G^<(z,z',E) \tag{5b}$$

$$\begin{aligned} U_n(z) = \sigma \int \frac{dE}{2\pi\hbar} \int dz' \big[&\Sigma^R(z,z',E)G^<(z',z,E) \\ &+ \Sigma^<(z,z',E)G^A(z',z,E) \\ &- G^R(z,z',E)\Sigma^<(z',z,E) \\ &- G^<(z,z',E)\Sigma^A(z',z,E)\big], \end{aligned} \tag{5c}$$

where $\sigma = 2$ accounts for spin degeneracy. The transverse wave number k is omitted in the arguments of Keldysh field components since we assume ($O = G, \Sigma$) [29]

$$O^{R,A}(k,z,z';E) = O^{R,A}(z,z';E - E_k), \tag{6}$$

and integration over transverse wave vectors is understood. In a multiband context, the scattering component of U_n is zero if the energy integration is taken over both valence and conduction bands, assuming that the self-energies are computed within a current-conserving scheme such as the self-consistent Born approximation (SCBA). If the integration is restricted to one of the bands, one finds the (net) recombination rate [28]. In the present single-band framework, interband transitions can be included by means of semiclassical generation and recombination rates [27,30]. In the following, we restrict our attention to unipolar carrier transport, so the only contribution that survises in Eq. (5c) is the one associated to the boundary self-energy expressing the openness of the system.

The retarded and lesser Green's functions are given by the self-consistent solution of the Dyson and Keldysh equations

$$\begin{aligned} G^R(z,z',E) = G_0^R(z,z',E) + \int dz_1 \int dz_2\, G_0^R(z,z_1,E) \\ \times \Sigma^R(z_1,z_2,E)G^R(z_2,z',E) \end{aligned} \tag{7a}$$

$$\begin{aligned} G^<(z,z',E) = \int dz_1 \int dz_2\, G^R(z,z_1,E) \\ \times \Sigma^<(z_1,z_2,E)G^A(z_2,z',E), \end{aligned} \tag{7b}$$

where G_0^R is Green's function of the noninteracting system. The retarded Green's function provides the local density of states (LDOS) while the lesser Green's function describes how the states are occupied and determines the relevant one-particle properties. Finite-element (FE) approaches for the numerical discretization of Eq. (7) are generally more accurate than finite-difference (FD) schemes, especially near the contacts and in the presence of doping discontinuities [31]. However, for clearness, we employ a FD scheme for the discretization of the model equations, as the use of nonorthogonal FE basis functions would lead to lengthy expressions of the Jacobian matrix elements. We also assume a constant effective mass and a uniform mesh with spacing Δ (a simple matrix transformation allows the use of nonuniform meshes in FD schemes preserving the symmetries of Green's functions [32]). The FD version of Eq. (7) is

$$G^R(E) = \left[E\mathbf{1} - H - \Sigma^R(E)\right]^{-1} \tag{8a}$$

$$G^<(E) = G^R(E)\Sigma^<(E)G^A(E), \tag{8b}$$

where $G^A = (G^R)^\dagger$, $\mathbf{1}$ is the identity matrix, and H is the (tridiagonal) Hamiltonian matrix (subscript i denotes nodal quantities)

$$\begin{aligned} H_{ii} &= \hbar^2/(m_n^*\Delta^2) - e\phi_i + \Delta E_{C,i} \\ H_{ii\pm1} &= -\hbar^2/(2m_n^*\Delta^2). \end{aligned} \tag{9}$$

A. Interaction self-energies

The computational burden of NEGF models is mainly related to the nonlocal nature of the relevant scattering processes and/or to the difficulty in achieving self-consistency between self-energies and Green's functions in the presence of strong localization effects [33]. In particular, the coupling of the Dyson and Keldysh equations makes any retarded self-energy associated with an inelastic-scattering mechanism dependent on both retarded and lesser Green's functions [34]. Originally introduced as a phenomenological scattering model—equivalent to the relaxation time approximation in the semiclassical Boltzmann transport equation—the formalism based on Büttiker probes was extended to provide a rigorous description of carrier-phonon scattering within the SCBA, decoupling the calculation of retarded self-energies from lesser Green's functions [29,35]. Following Ref. [35] and neglecting renormalization effects, we model deformation potential scattering assisted by acoustic and optical phonons with the following (local) self-energies compatible with

ansatz (6)

$$\Sigma^R_{\mathrm{aco},ii}(E) = \frac{D^2_{\mathrm{aco}} k_B T}{\rho_m v_s^2 a_{\mathrm{lat}}} N_{2D} i\, \mathbb{I}m\left\{G^R_{ii}(E)\right\} \tag{10a}$$

$$\Sigma^R_{\mathrm{opt},ii}(E) = \frac{\hbar D^2_{\mathrm{tK}}}{2\rho_m \omega_q a_{\mathrm{lat}}} \tag{10b}$$

$$\times \left[(n_{\mathrm{ph}} E_{\max} + \mathcal{F}_0(E^+, \mu_{n,i}) i\, \mathbb{I}m\left\{G^R_{ii}(E^+)\right\} + (n_{\mathrm{ph}} + 1)E_{\max} - \mathcal{F}_0(E^-, \mu_{n,i})\, i\, \mathbb{I}m\left\{G^R_{ii}(E^-)\right\}\right], \tag{10c}$$

where $\mu_{n,i}$ is the Fermi level of the ith Büttiker probe, n_{ph} is the number of phonons computed according to Boson statistics, D_{tK} is the optical deformation potential, ρ_m is the density of the material, a_{lat} is the lattice constant, D_{aco} is the acoustic deformation potential, v_s is the sound velocity, $N_{2\mathrm{D}} = m^*_n/(2\pi\hbar^2)$ is the two-dimensional density of states, $E^{\pm} = E \pm E_{\mathrm{ph}}$, E_{ph} is the optical phonon energy, and

$$\mathcal{F}_0(E, \mu) = N_{2\mathrm{D}} k_B T \log\left[\frac{1 + \exp\left(\frac{\mu - E}{k_B T}\right)}{1 + \exp\left(\frac{\mu - E - E_{\max}}{k_B T}\right)}\right] \tag{11}$$

results from the integration of the Fermi-Dirac function up to a maximum transverse energy $E_{\max} = \hbar^2 k^2_{\max}/(2m^*_n)$ [36,37]. An implicit assumption in the Büttiker probe formalism (and also one of the tenets of DD approaches) is the existence of a local quasiequilibrium, which allows the use of a local version of the fluctuation-dissipation theorem [38] to compute the lesser component of the scattering self-energy

$$\Sigma^<_{\mathrm{BP},ii}(E) = i\mathcal{F}_0(E, \mu_{n,i})\Gamma_{\mathrm{BP},ii}(E), \tag{12}$$

where $\Gamma_{\mathrm{BP}} = i\left(\Sigma^R_{\mathrm{BP}} - \Sigma^A_{\mathrm{BP}}\right)$ is the broadening function associated to $\Sigma_{\mathrm{BP}} = \Sigma_{\mathrm{aco}} + \Sigma_{\mathrm{opt}}$.

B. Incoherent carrier injection

Reflectionless boundaries are essential if local charge neutrality is expected at the contacts [39]. In most NEGF implementations, the contacts are treated in the coherent limit, but, when scattering processes are included in the device region, the coherent injection of carriers leads to an artificial band bending near the reservoirs in self-consistent potential calculations [34]. A similar effect has been observed in dissipative phonon transport simulations, in which the phonon population appears reasonable only if incoherent phonons are injected by the contacts [40]. Artefacts related to the coherent injection of carriers are particularly undesirable in small-signal calculations, since the frequency response may be controlled by the contacts rather than by the device under study. Assuming in the left contact a constant and local scattering self-energy equal to $\Sigma^R_{\mathrm{BP},11}$, the recursive relation for the boundary self-energy gives ($h = E\mathbf{1} - H$) [41]

$$\Sigma^R_L(E) = \frac{h_{11} - \Sigma^R_{\mathrm{BP},11} \pm \sqrt{\left(h_{11} - \Sigma^R_{\mathrm{BP},11}\right)^2 - 4h^2_{12}}}{2} \tag{13}$$

$$\Sigma^<_L(E) = i\mathcal{F}_0(E, \mu_L)\, \Gamma_L(E). \tag{14}$$

Similar expressions hold for the boundary self-energy Σ^R_R at the right contact. The choice of the sign in Eq. (13) is determined by the requirement $\mathbb{I}m\left\{\Sigma^R_{L,R}\right\} < 0$ for a casual Green's function.

C. Equilibrium

At equilibrium, the continuity equation is satisfied by the fluctuation-dissipation theorem, and we are left with the nonlinear Poisson equation defined by the functional

$$F_{\phi,i} = \sum_j P_{ij}\phi^{(\mathrm{eq})}_j + \frac{\sigma}{\Delta}\int \frac{dE}{2\pi}\mathcal{F}_0(E, \mu)A_{ii}(E) - N_{\mathrm{D},i} = 0, \tag{15}$$

where $A_{ii} = i(G^R_{ii} - G^A_{ii})$ are the diagonal elements of the spectral function (i.e., the LDOS), $\mu = \mu_{L,R} = 0$, and P is the tridiagonal stiffness matrix

$$\begin{aligned} P_{ii} &= (\varepsilon_{i-1} + 2\varepsilon_i + \varepsilon_{i+1})/\Delta^2 \\ P_{ii\pm1} &= -(\varepsilon_i + \varepsilon_{i\pm1})/\Delta^2. \end{aligned} \tag{16}$$

Implicit in Eq. (15) are zero-field BCs, which let the potential float to ensure global charge neutrality, and define the built-in potential across the device. If the homogeneous device region close to the boundaries is large enough, the condition of vanishing electric fields entails the local charge neutrality [34]. Gummel algorithms for the minimization of Eq. (15) may take thousands of iterations to converge, if at all. Prediction-correction schemes provide improved, but less-than-quadratic convergence, and, crucially, they are not suited for small-signal analysis [22]. Therefore, we propose a Newton-Raphson scheme based on the numerical evaluation of functional derivatives [27]. Since the Jacobian of Eq. (15) is a subset of the full Jacobian employed in steady-state calculations, we refer to the next section for details.

D. Steady-state analysis

In steady-state conditions, the model Eq. (4) reads in residual form

$$F_{\phi,i} = \sum_j P_{ij}\phi_j + \frac{-i\sigma}{\Delta}\int \frac{dE}{2\pi} G^<_{ii}(E) - N_{D,i} = 0 \quad (17a)$$

$$F_{\mu_{n,i}} = \frac{\sigma}{\Delta}\int \frac{dE}{2\pi\hbar}\, 2\mathbb{R}e\left\{HG^<(E)\right\}_{ii} + U_{n,i} = 0. \quad (17b)$$

As discussed earlier, U_n represents the recombination rate due to interband transitions connecting conduction and valence bands, but it also includes charge injection and extraction at the contacts. Choosing the right contact as the reference terminal, we ensure that the applied voltage V drops entirely across the device, by imposing Dirichlet BCs for the electrostatic potential and the quasi-Fermi-level [42,43]

$$F_{\phi,1} = \phi_1 - \phi_1^{(\mathrm{eq})} - V = 0 \quad (18a)$$

$$F_{\phi,N} = \phi_N - \phi_N^{(\mathrm{eq})} = 0 \quad (18b)$$

$$F_{\mu_n,1} = \mu_{n,1} + eV = 0 \quad (18c)$$

$$F_{\mu_n,N} = \mu_{n,N} = 0. \quad (18d)$$

Assuming the contacts at equilibrium with Fermi levels $\mu_L = \mu_{n,1}$, $\mu_R = \mu_{n,N}$, the solution of the system (17) and (18) leads to a charge imbalance near the contacts when a sizeable current flows, which indicates that current conservation is not verified at device-contact boundaries. Indeed, as equilibrium contacts carry no current, current continuity is clearly violated. However, restricting our attention to the device region, the local charge neutrality can be recovered by "adjusting" the Fermi levels of the contacts so that the local divergence of the current is zero also at the boundary nodes, according to the supplementary equations

$$F_{\mu_L} = \frac{\sigma}{\Delta}\int \frac{dE}{2\pi\hbar}\, 2\mathbb{R}e\left\{HG^<(E)\right\}_{11} + U_L = 0 \quad (19a)$$

$$F_{\mu_R} = \frac{\sigma}{\Delta}\int \frac{dE}{2\pi\hbar}\, 2\mathbb{R}e\left\{H\, G^<(E)\right\}_{NN} + U_R = 0, \quad (19b)$$

where $U_{L,R}$ are recombination terms arising from the boundary self-energies encoded in $G^<$

$$U_L = \frac{\sigma}{\Delta}\int \frac{dE}{2\pi\hbar} 2\mathbb{R}e\left\{G^R_{11}(E)\Sigma^<_L(E) - G^<_{11}(E)\Sigma^R_L(E)\right\} \quad (20a)$$

$$U_R = \frac{\sigma}{\Delta}\int \frac{dE}{2\pi\hbar} 2\mathbb{R}e\left\{G^R_{NN}(E)\Sigma^<_R(E) - G^<_{NN}(E)\Sigma^R_R(E)\right\}. \quad (20b)$$

In other words, we describe charge injection by means of the boundary generation and recombination rates $U_{L,R}$. These recombination terms are not included in Büttiker-probe models, the "incomplete" continuity equations at the boundary nodes simply provided the terminal currents. Contacts with adjusted Fermi levels were originally introduced in quantum transport calculations with scattering states [44]. Alternative, but phenomenologically equivalent, current-conserving approaches have been proposed in the context of quantum and semiclassical device simulation, e.g., displaced or shifted distributions along the longitudinal momentum [34,45,46], or velocity-weighted distributions [47]. We favor equilibrium distributions with adjusted Fermi levels, since they are compatible with the fluctuation-dissipation expression (14).

Before we proceed with the linearization procedure, it is convenient to add two additional equations to enable mixed-mode device and circuit simulations [48]. Assuming that the device is driven by a real voltage source, we have

$$F_V = V + R_s I - V_{\mathrm{bias}} = 0 \quad (21)$$

$$F_I = I - e\Delta\, U_L = 0, \quad (22)$$

where R_s is the generator series resistance, V_{bias} is the generator open-circuit voltage, and I is the current entering the left contact. If the device is driven by a current source, the circuit Eq. (21) should be replaced with

$$F_V = I + G_p V - I_{\mathrm{bias}}, \quad (23)$$

where G_p is the generator parallel conductance and I_{bias} is the generator short-circuit current. The simple functional dependence of Green's functions and self-energies on the unknowns

$$x = (\{\phi_i\}, \{\mu_{n,i}\}, \mu_L, \mu_R, V, I)^T \quad (24)$$

allows closed-form expressions for the Jacobian matrix elements.

As an example, we report the derivatives of Eq. (17) with respect to the electrostatic potential. Using the chain derivation rule and the derivative of the inverse matrix, we find (for brevity, we omit the parametric dependence on E)

$$\frac{\partial G^R}{\partial \phi_j} = G^R \frac{\partial (H + \Sigma^R)}{\partial \phi_j} G^R \quad (25a)$$

$$\frac{\partial G^<}{\partial \phi_j} = \frac{\partial G^R}{\partial \phi_j}\Sigma^< G^A + G^R \frac{\partial \Sigma^<}{\partial \phi_j} G^A + G^R \Sigma^< \frac{\partial G^A}{\partial \phi_j}, \quad (25b)$$

which delivers

$$\frac{\partial F_{\phi,i}}{\partial \phi_j} = P_{ij} - \frac{i\sigma}{\Delta}\int \frac{dE}{2\pi}\left[G^R \frac{\partial \Sigma^<}{\partial \phi_j} G^A + 2i\mathbb{I}m\left\{G^R \frac{\partial (H + \Sigma^R)}{\partial \phi_j} G^<\right\}\right]_{ii} \quad (26a)$$

$$\frac{\partial F_{\mu_n,i}}{\partial \phi_j} = \frac{\sigma}{\Delta}\int \frac{dE}{2\pi\hbar} 2\mathbb{R}e\left\{H\left[G^R\frac{\partial \Sigma^<}{\partial \phi_j}G^A + G^R\frac{\partial \Sigma^R}{\partial \phi_j}G^< + G^<\frac{\partial \Sigma^A}{\partial \phi_j}G^A\right]\right\}_{ii} + \frac{\partial U_{n,i}}{\partial \phi_j}, \tag{26b}$$

where we use the symmetry properties of Green's functions.

The derivatives of the scattering self-energies depend on the derivatives of the diagonal elements of the retarded Green's function, e.g.,

$$\frac{\partial \Sigma^R_{\text{aco},ii}}{\partial \phi_j} = \frac{D^2_{\text{aco}} k_B T}{\rho_m v_s^2 a_{\text{lat}}} N_{2D} i\,\mathbb{I}m\left\{\frac{\partial G^R_{ii}}{\partial \phi_j}\right\} \tag{27a}$$

$$\frac{\partial \Sigma^<_{\text{aco},ii}}{\partial \phi_j} = i\frac{\partial \Gamma_{\text{aco},ii}}{\partial \phi_j}\mathcal{F}_0(E,\mu_{n,i}), \tag{27b}$$

which can be expressed again in terms of Hamiltonian and self-energy derivatives, see Eq. (25a).

So, the evaluation of the Jacobian requires the calculation of the diagonal elements of products of the type $G_1\ (\partial X/\partial\phi)\ G_2$, where X is the Hamiltonian or a self-energy matrix and $G_{1,2}$ are Green's functions. Since all self-energies are local in space and the electrostatic potential appears only in the diagonal of H, we find

$$\left[G_1(\,\partial X/\partial\phi_j)\,G_2\right]_{ii} = \left[(G_1 \circ G_2^T)\,X'\right]_{ij}, \tag{28}$$

where $\circ$ is the Hadamard or elementwise product, and X' is a matrix whose columns are the diagonals of $\partial X/\partial\phi_j$. Having computed the Jacobian matrix, the Newton-Raphson update δx can be computed by solving the linear system

$$\sum_\beta \frac{\partial F_\alpha}{\partial x_\beta}\,\delta x_\beta = -F_\alpha. \tag{29}$$

In total, Eq. (29) includes $2N+4$ equations in $2N+2$ physical unknowns and two circuit unknowns.

E. Small-signal analysis

Small-signal analysis means finding the relationship between small sinusoidal terminal currents and voltages superimposed upon an established steady-state working point [49]. Here "small" means in the limit of infinitesimal amplitude, so that no harmonic generation occurs within the device. For periodically driven systems, Green's functions and self-energies can be expanded in Floquet series [50] ($O^\gamma = G^\gamma, \Sigma^\gamma$)

$$O^\gamma(t,t') = \sum_l \int \frac{dE}{2\pi\hbar} O^\gamma_l(E) e^{-iE(t-t')/\hbar} e^{-il\omega t}. \tag{30}$$

Restricting the Floquet series to first-order harmonics, i.e., assuming

$$O^\gamma(E,t) = O^\gamma(E) + \tilde{O}^\gamma(E)e^{i\omega t}, \tag{31}$$

where O^γ is a steady-state solution and $\tilde{O}^\gamma$ is a small-signal perturbation, one finds in the linear response limit ($\bar{E} = E - \hbar\omega$) [14,18]

$$\tilde{G}^R(E) = G^R(\bar{E})[\tilde{H} + \tilde{\Sigma}^R(\bar{E})]G^R(E) \tag{32a}$$

$$\tilde{G}^<(E) = \tilde{G}^R(\bar{E})\Sigma^<(E)G^A(E) + G^R(\bar{E})\tilde{\Sigma}^<(\bar{E})G^A(E) + G^R(\bar{E})\Sigma^<(\bar{E})\tilde{G}^A(\bar{E}). \tag{32b}$$

At subterahertz frequencies, say, at 100 GHz, the energy corresponding to the ac driving frequency would be approximately 0.4 meV, which in most cases is less than the scattering-induced broadening (in all the calculations presented in this work, fully scattered Green's functions have been computed with an energy resolution of 5 meV). Therefore, we neglect photon emission and absorption processes by replacing $\bar{E}$ with E in the arguments of Green's functions and self-energies. Then, Eq. (32) corresponds to Eq. (25), and the small-signal version of Eq. (29) can be symbolically written as

$$\sum_\beta \left(\frac{\partial F_\alpha}{\partial x_\beta} + \frac{\partial D_\alpha(\omega)}{\partial x_\beta}\right)\tilde{x}_\beta = b_\alpha, \tag{33}$$

where b_V includes the ac voltage drive, and the frequency-dependent matrix D accounts for the displacement current in the continuity Eq. (17b)

$$D_{\mu_n,i}(\omega) = i\omega\frac{-i\sigma}{\Delta}\int\frac{dE}{2\pi}G^<_{ii}(E), \tag{34}$$

and in the current equation (22)

$$D_I(\omega) = i\omega(P_{11}\phi_1 + P_{12}\phi_2). \tag{35}$$

The algorithm for the calculation of the small-signal admittance at a given steady-state solution can be summarized as follows.

1. Start with an initial guess from a steady-state solution at a previous voltage; if not available, use the ballistic solution at equilibrium. Let x_n be the array of the unknowns at the nth Newton iteration. By "solution" we mean the

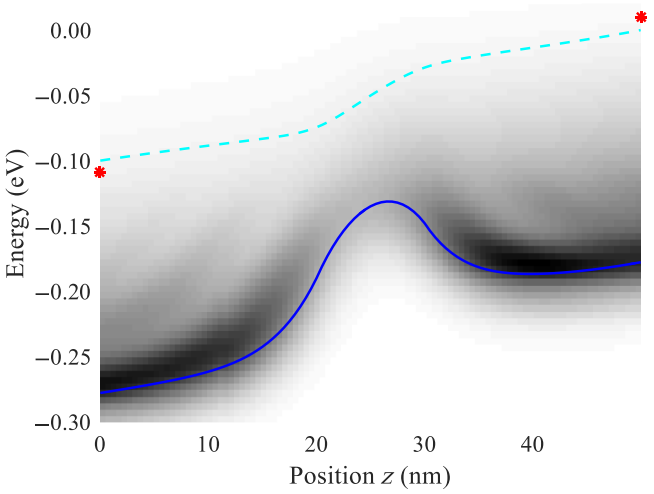

FIG. 1. Spectral electron density (grayscale) and band diagram of a GaAs *n-i-n* structure computed for an applied bias of $V = 0.1$ V, with current-conserving BCs and incoherent injection from the contacts. The adjusted Fermi levels of the contacts (red asterisks) are slightly shifted with respect to the quasi-Fermi-levels at device-contact boundaries. The shift is proportional to the current flowing through the structure.

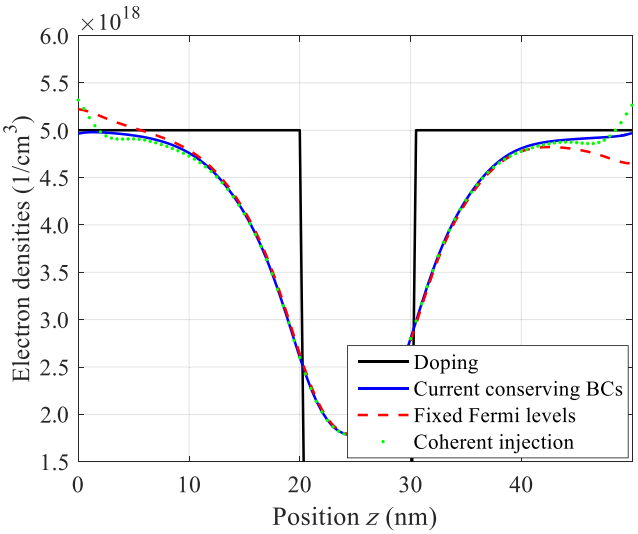

FIG. 2. Doping profile (black solid line) and energy-integrated electron densities computed with current-conserving BCs and incoherent injection (blue solid line), Fermi levels of the contacts fixed to the value of the quasi-Fermi-levels at device-contact boundaries and incoherent injection (red dashed line), current-conserving BCs and coherent injection (green dotted line). The material parameters used in all simulations are $m_n^* = 0.067m_0$, $D_{\text{tK}} = 3 \times 10^9$ eV/cm, $\rho_m = 5.32$ g/cm^3, $a_{\text{lat}} = 0.5$ nm, $D_{\text{aco}} = 10$ eV, $v_s = 6.56$ km/s, and $E_{\text{ph}} = 30$ meV.

array x of the unknowns and the diagonals of G^R at all energy points. A uniform energy grid is assumed (the present approach is compatible with self-adaptive energy discretization techniques [51]).

2. For a given energy E, evaluate the retarded scattering self-energies Σ^R_{BP} using the previously calculated retarded Green's functions. Extend the values of Σ^R_{BP} at device-contact boundaries to the reservoirs and compute the boundary self-energies $\Sigma^R_{L,R}$. Then, solve the Dyson Eq. (8a) for G^R; save the diagonals of G^R and their derivatives with respect to the unknowns.

3. Go back to step 2 to achieve self-consistency between G^R and Σ^R_{BP} (inner loop).

4. For a given energy E, solve the Keldysh Eq. (8b) for $G^<$.

5. Compute the scattering self-energy derivatives from Green's function derivatives saved at step 2. Integrate all functional derivatives over energy, and solve the linearized system (29) to obtain the updated solution $x_{n+1} = x_n + \delta x_n$.

6. Go back to step 2 until $||x_{n+1} - x_n||$ is less than a given tolerance (outer loop).

7. Add the frequency-dependent matrix D to the last computed steady-state Jacobian and solve the small-signal system (33) for $\tilde{x}$. The small-signal admittance is given by $\tilde{I}/\tilde{V}$.

In conventional NEGF implementations, the "inner" loop is employed to achieve self-consistency between Green's functions and self energies, while the "outer" loop provides the update of the Hartree potential from the solution of Poisson's equation. Here, thanks to the decoupling of the Dyson and Keldysh equations, only retarded Green's

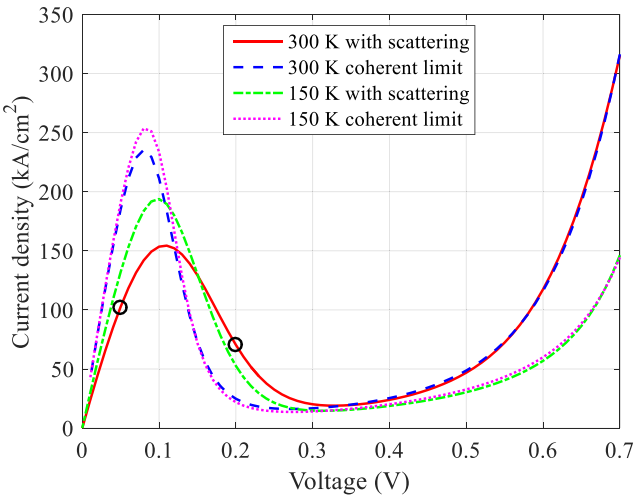

FIG. 3. I-V characteristics of a typical *n-i-n* RTD, computed at $T = 150$ K and $T = 300$ K in the coherent limit and in the presence of scattering processes. The black circles mark two steady-state working points in the PDR and NDR regions selected for the small-signal analysis.

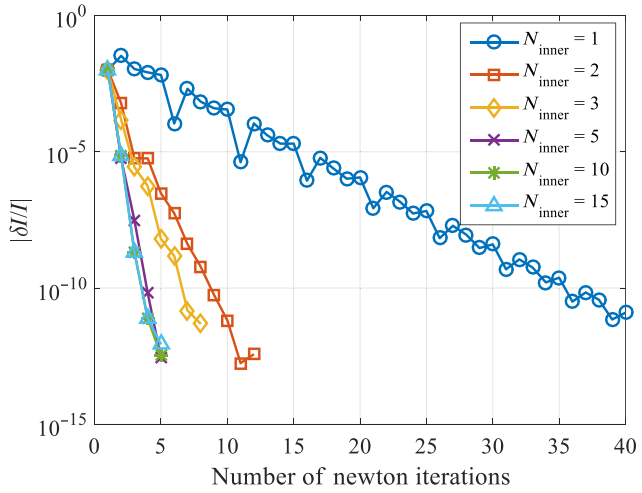

FIG. 4. Convergence of the terminal current for different numbers of inner iterations, when the applied bias is changed from 0.2 V to 0.25 V.

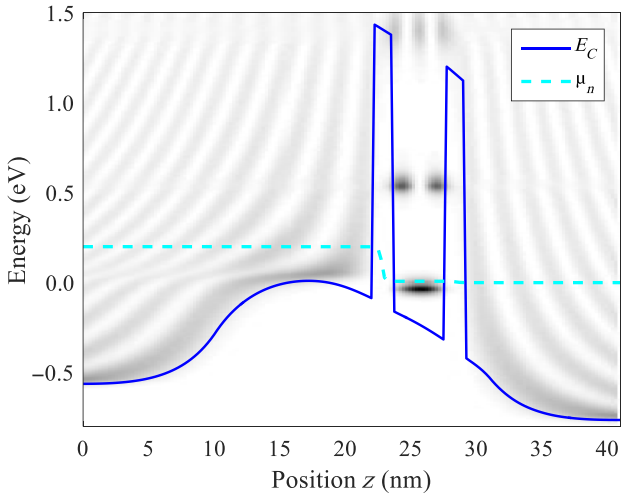

FIG. 5. Spectral LDOS (grayscale) of the RTD biased in NDR region ($V_{\text{bias}} = 0.2$ V, $T = 300$ K). The quasi-Fermi-level (cyan dashed line) is constant in the quantum well, which supports the common assumption that a quasi-equilibrium population of electrons exists between the barriers.

functions are converged in the inner loop, while the electrostatic potential and the quasi-Fermi-levels are updated by means of a Newton-Raphson scheme (outer loop) to meet current conservation requirements.

III. RESULTS

We first illustrate the relevance of current conservation at device-contact boundaries by considering a GaAs *n-i-n* resistive structure consisting of a lightly doped ($N_D = 10^{16}$ cm^{-3}) region of thickness 10 nm embedded between 15-nm-thick heavily doped layers ($N_D = 5 \times 10^{18}$ cm^{-3}). Figure 1 shows the band diagram computed for a bias voltage of 0.1 V, with the current-conserving BCs (19) and with incoherent injection from the contacts. The red asterisks mark the positions of the adjusted contact Fermi levels that ensure current conservation. No reflections from the contacts can be seen in the electron spectral density. The energy-integrated electron densities computed with different BCs are shown in Fig. 2. The current-conserving BCs (19) provide the expected behavior near the contacts (blue solid line). If we impose $\mu_L = \mu_{n,1}$ and $\mu_R = \mu_{n,N}$, a discontinuity appears in the quasi-Fermi-level near the contacts, which leads, via the Poisson feedback, to electron accumulation or depletion at the device-contact boundaries (red dashed lines). A similar effect is observed with current-conserving BCs if scattering is neglected in the reservoirs (green dotted line). In this case the charge imbalance is already present at equilibrium.

We now consider a typical RTD consisting of a 5-nm $In_{0.53}Ga_{0.47}As$ quantum well between 1.5-nm-thick AlAs barriers. The intrinsic double-barrier quantum well heterostructure is embedded in lightly doped spacer layers (20 nm, $N_D = 10^{17}$ cm^{-3}), followed by heavily doped contact layers (20 nm, $N_D = 10^{19}$ cm^{-3}). Originally investigated to verify the predictions of quantum transport models, RTDs have found application in the fields of high-speed terahertz wireless communications [52], high-resolution imaging [53], and single-photon counting [54]. The current-voltage curve of a RTD is highly nonlinear

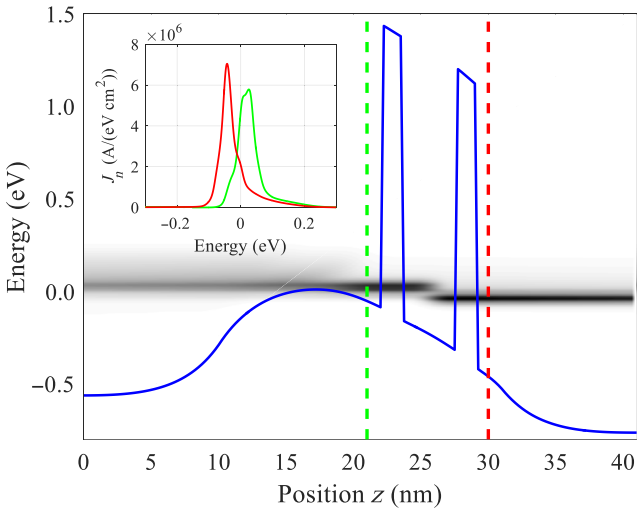

FIG. 6. Two strips of spectral current density (grayscale) reach the quantum well region from opposite sides at slightly displaced energies, which is indicative of sequential tunneling assisted by phonon emission processes. The sudden interruption in the otherwise almost coherent propagation of the tunneling electrons is better appreciated in the inset, which shows cuts of the spectral current density at the positions marked by the vertical dashed lines. Calculations are performed in the NDR region at $V_{\text{bias}} = 0.2$ V and $T = 300$ K.

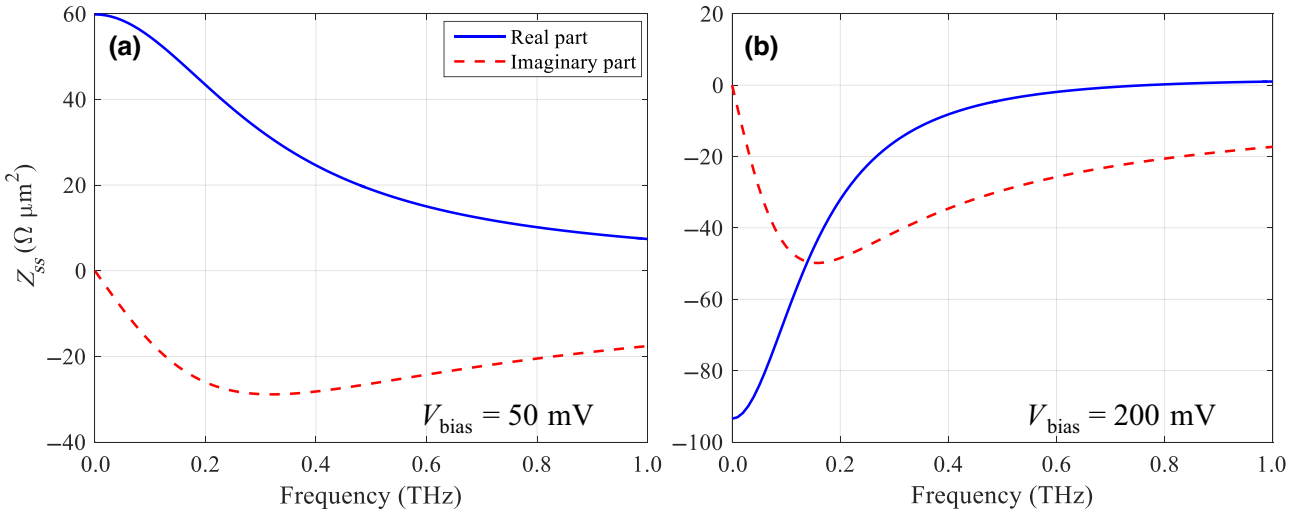

FIG. 7. Real (blue solid lines) and imaginary (red dashed lines) parts of the small-signal impedance versus frequency, computed at a bias voltage of 0.05 V (left panel) and 0.2 V (right panel), in the PDR and NDR regions, respectively. Calculations are performed at $T = 300$ K.

and characterized by a number of resonances, occurring whenever tunneling across a (quasi)bound state of the nanostructure is enabled by energy alignments. In the context of terahertz emitters, the maximum RF power that can be delivered to a load depends on the precise shape of the negative differential resistance (NDR) region. On the other hand, single-photon detectors are usually operated in the positive differential resistance (PDR) region, and the photocurrent depends on the shift of the current-voltage characteristics due to the accumulation of photogenerated holes in the vicinity of the quantum well (phototransistor effect).

Although resonant tunneling is a purely ballistic mechanism, carrier transport is not entirely coherent in a RTD. Figure 3 shows the steady-state I-V curve of the RTD, computed with and without scattering mechanisms, at different temperatures. Scattering with phonons leads to a wider resonance and to a less pronounced peak compared to ballistic simulations [55]. As in a superlattice, carrier-phonon scattering reduces the resonant contribution of the current and enhances the nonresonant one by opening additional channels not accessible to ballistic propagation [5]. Carrier-phonon scattering also explains the temperature dependence of the I-V characteristics, as the scattering self-energy is proportional to the phonon occupation number. Different temperature behaviors have been reported in the literature of RTDs: in some structures, the NDR completely disappears at high temperatures due to thermionic emission or other thermally activated transport mechanisms such as defect hopping [56,57], but temperature-insensitive I-V characteristics have also been reported [58]. In the device under study, the reduction of the peak current for increasing temperature can be almost entirely attributed to carrier-phonon scattering and to the resulting broadening of the resonant states. The ballistic simulations in Fig. 3 indicate that energy alignments and the thermal smearing of the emitter electron distribution play a minor role, while inspection of the spectral current shows that thermionic emission is effectively blocked by the AlAs barriers in the bias range investigated.

Figure 4 shows a typical evolution of the current update during the outer (Newton) loop for different numbers of inner iterations. The inner loop is not strictly necessary, as convergence is ensured by the outer loop, but few inner iterations improve the stability of the algorithm and decrease the computation time. Inspection of the LDOS and the spectral current density reveals that sequential tunneling is the dominant transport mechanism in the NDR region, see Figs. 5 and 6. Indeed, the sharp downshift of the spectral current in the resonance region, see inset, is indicative of relatively intense scattering in the quantum well compared to the leads [59]. The existence of a local equilibrium in the quantum well is revealed by a constant quasi-Fermi-level between the barriers, see Fig. 5. The inclusion of scattering processes is also useful for the accurate determination of the intrinsic cutoff frequency of the RTD, as the electron lifetime in the quantum well depends on the strength of the scattering mechanisms connecting the localized states in the quantum well with the delocalized current-carrying states in the emitter and collector regions. The frequency dependence of the real and imaginary parts of the small-signal impedance in the PDR and NDR regions are reported in Fig. 7. Our results are in qualitative agreement with time-dependent quantum Monte Carlo calculations based on Bohmian trajectories [60], and equivalent circuit models obtained from scattering parameter measurements [61]. The small-signal conductance equals the differential conductance in the low-frequency

limit, while in the high-frequency limit, the capacitance approaches the geometrical capacitance. Conservation of the total current (particle plus displacement) is always satisfied.

IV. CONCLUSION

We present an accurate, yet computationally efficient NEGF model of dissipative carrier transport in nanodevices, with current-conserving and reflectionless contacts. The linearization of the model equations ensures the fast convergence of steady-state calculations and provides information on the small-signal carrier transport properties of nanostructures at subterahertz frequencies. The model can be extended to the bipolar case by means of appropriate generation and recombination rates to describe interband processes, with potential application to advanced optoelectronic devices such as T2SL photodetectors. This work lays the foundation for sensitivity, variability, and noise studies in quantum systems, with microscopic (electrical or geometrical) fluctuations as small perturbations with respect to a steady-state solution [62–64].

ACKNOWLEDGMENTS

This work is partially supported by the European Union – Next Generation EU under the Italian National Recovery and Resilience Plan (PNRR M4C2, Investimento 1.4 - Avviso n. 3138 del 16/12/2021 - CN00000013 National Centre for HPC, Big Data and Quantum Computing (HPC) - CUP E13C22000990001), by AreaIT@PoliTO through the Cloud service, and by the photonics technology center PhotoNext@PoliTO.

[1] B. Chen, Y. Chen, and Z. Deng, Recent advances in high speed photodetectors for eSWIR/MWIR/LWIR applications, MDPI Photon. **8**, 14 (2021).

[2] J. Huang, Z. Shen, Z. Wang, Z. Zhou, Z. Wang, B. Peng, W. Liu, Y. Chen, and B. Chen, High-speed mid-wave infrared uni-traveling carrier photodetector based on InAs/InAsSb type-II superlattice, IEEE Electron Device Lett. **43**, 745 (2022).

[3] R. Wan, L. Wang, J. Huang, X. Yi, H.-C. Kuo, and J. Li, Improving the modulation bandwidth of GaN-based light-emitting diodes for high-speed visible light communication: Countermeasures and challenges, Adv. Photon. Res. **2**, 2100093 (2021).

[4] A. Wacker, Semiconductor superlattices: a model system for nonlinear transport, Phys. Rep. **357**, 1 (2002).

[5] F. Bertazzi, A. Tibaldi, M. Goano, J. A. Gonzalez Montoya, and E. Bellotti, Non-Equilibrium Green's Function Modeling of Type-II Superlattice Detectors and its Connection to Semiclassical Approaches, Phys. Rev. Appl. **14**, 014083 (2020).

[6] G. Verzellesi, D. Saguatti, M. Meneghini, F. Bertazzi, M. Goano, G. Meneghesso, and E. Zanoni, Efficiency droop in InGaN/GaN blue light-emitting diodes: Physical mechanisms and remedies, J. Appl. Phys. **114**, 071101 (2013).

[7] M. Meneghini, C. De Santi, A. Tibaldi, M. Vallone, F. Bertazzi, G. Meneghesso, E. Zanoni, and M. Goano, Thermal droop in III-nitride based light-emitting diodes: physical origin and perspectives, J. Appl. Phys. **127**, 211102 (2020).

[8] M. Luisier, Atomistic simulation of transport phenomena in nanoelectronic devices, Chem. Soc. Rev. **43**, 4357 (2014).

[9] C. Jirauschek and T. Kubis, Modeling techniques for quantum cascade lasers, Appl. Phys. Rev. **1**, 011307 (2014).

[10] U. Aeberhard, Photovoltaics at the mesoscale: Insights from quantum-kinetic simulation, J. Phys. D **51**, 323002 (2018).

[11] F. Rossi, *Theory of Semiconductor Quantum Devices. Microscopic Modeling and Simulation Strategies* (Springer-Verlag, Berlin, 2011).

[12] M. Fischetti and W. G. Vandenberghe, *Advanced Physics of Electron Transport in Semiconductors and Nanostructures* (Springer-Verlag, Berlin, 2016).

[13] M. R. Hirsbrunner, T. M. Philip, B. Basa, Y. Kim, M. J. Park, and M. J. Gilbert, A review of modeling interacting transient phenomena with non-equilibrium Green functions, Rep. Prog. Phys. **82**, 046001 (2019).

[14] M. P. Anantram and S. Datta, Effect of phase breaking on the ac response of mesoscopic systems, Phys. Rev. B **51**, 7632 (1995).

[15] G. Platero and R. Aguado, Photon-assisted transport in semiconductor nanostructures, Phys. Rep. **395**, 1 (2004).

[16] T. Brandes, Truncation method for Green's functions in time-dependent fields, Phys. Rev. B **56**, 1213 (1997).

[17] D. O. Winge, M. Lindskog, and A. Wacker, Nonlinear response of quantum cascade structures, Appl. Phys. Lett. **101**, 211113 (2012).

[18] A. Wacker, M. Lindskog, and D. O. Winge, Nonequilibrium Green's function model for simulation of quantum cascade laser devices under operating conditions, IEEE J. Select. Top. Quantum Electron. **19**, 1200611 (2013).

[19] D. Kienle, M. Vaidyanathan, and F. Léonard, Self-consistent ac quantum transport using nonequilibrium Green functions, Phys. Rev. B **81**, 115455 (2010).

[20] S.-M. Hong and P.-H. Ahn, in *2020 International Conference on Simulation of Semiconductor Processes and Devices (SISPAD)*, Kobe, Sep. 2020, p. 289.

[21] P.-H. Ahn and S.-M. Hong, in *2021 IEEE International Electron Devices Meeting (IEDM)*, San Francisco, Dec. 2021, p. 410.

[22] P.-H. Ahn and S.-M. Hong, A fully coupled scheme for a self-consistent Poisson-NEGF solver, IEEE Trans. Electron Devices **70**, 239 (2023).

[23] B. Wang, J. Wang, and H. Guo, Current Partition: A Nonequilibrium Green's Function Approach, Phys. Rev. Lett. **82**, 398 (1999).

[24] Y. Wei and J. Wang, Current conserving nonequilibrium ac transport theory, Phys. Rev. B **79**, 195315 (2009).

[25] J. Wang, Time-dependent quantum transport theory from non-equilibrium Green's function approach, J. Comp. Electron. **12**, 343 (2013).

[26] T. M. Philip and M. J. Gilbert, Theory of AC quantum transport with fully electrodynamic coupling, J. Comp. Electron. **17**, 934 (2018).

[27] A. Tibaldi, J. A. Gonzalez Montoya, M. Vallone, M. Goano, E. Bellotti, and F. Bertazzi, Modeling Infrared Superlattice Photodetectors: From Nonequilibrium Green's Functions to Quantum-Corrected Drift Diffusion, Phys. Rev. Appl. **16**, 044024 (2021).

[28] U. Aeberhard, Quantum-kinetic theory of photocurrent generation via direct and phonon-mediated optical transitions, Phys. Rev. B **84**, 035454 (2011).

[29] P. Greck, S. Birner, B. Huber, and P. Vogl, Efficient method for the calculation of dissipative quantum transport in quantum cascade lasers, Opt. Exp. **23**, 6587 (2015).

[30] K. Wang, R. Grassi, Y. Chu, S. H. Sureshbabu, J. Geng, P. Sarangapani, X. Guo, M. Townsend, and T. Kubis, Introduction of multi-particle Büttiker probes–Bridging the gap between drift-diffusion and quantum transport, J. Appl. Phys. **128**, 014302 (2020).

[31] H. Jiang, S. Shao, W. Cai, and P. Zhang, Boundary treatments in non-equilibrium Green's function (NEGF) methods for quantum transport in nano-MOSFETs, J. Comp. Phys. **227**, 6553 (2008).

[32] I.-H. Tan, G. L. Snider, L. D. Chang, and E. L. Hu, A self-consistent solution of Schrödinger-Poisson equations using a nonuniform mesh, J. Appl. Phys. **68**, 4071 (1990).

[33] U. Aeberhard, Quantum transport simulation of hot carrier photocurrent generation in quantum well solar cells, Semicond. Sci. Technol. **34**, 094002 (2019).

[34] T. Kubis and P. Vogl, Assessment of approximations in nonequilibrium Green's function theory, Phys. Rev. B **83**, 195304 (2011).

[35] J. A. Vaitkus and J. H. Cole, Büttiker probes and the recursive Green's function: an efficient approach to include dissipation in general configurations, Phys. Rev. B **97**, 085149 (2018).

[36] M. Goano, Series expansion of the Fermi-Dirac integral $\mathcal{F}_j(x)$ over the entire domain of real j and x, Solid-State Electron. **36**, 217 (1993).

[37] M. Goano, Algorithm 745. Computation of the complete and incomplete Fermi-Dirac integral, ACM Trans. Math. Softw. **21**, 221 (1995).

[38] V. Špička, B. Velický, and A. Kalvová, Non-equilibrium dynamics of open systems and fluctuation-dissipation theorems, Fortschr. Phys. **65**, 1700032 (2017).

[39] M. Frey, A. Esposito, and A. Schenk, in *2009 13th International Workshop on Computational Electronics*, Beijing, China, Jun. 2009.

[40] M. Luisier, Atomistic modeling of anharmonic phonon-phonon scattering in nanowires, Phys. Rev. B **86**, 245407 (2012).

[41] J. Velev and W. Butler, On the equivalence of different techniques for evaluating the Green function for a semi-infinite system using a localized basis, J. Phys. Condens. Matter **16**, R637 (2004).

[42] R. Venugopal, S. Goasguen, S. Datta, and M. S. Lundstrom, Quantum mechanical analysis of channel access geometry and series resistance in nanoscale transistors, J. Appl. Phys. **95**, 292 (2004).

[43] A. Shedbalkar and B. Witzigmann, Non equilibrium Green's function quantum transport for green multi-quantum well nitride light emitting diodes, Opt. Quantum Electron. **2/2018**, 67 (2018).

[44] W. Pötz, Self-consistent model of transport in quantum well tunneling structures, J. Appl. Phys. **66**, 2458 (1989).

[45] W. R. Frensley, Boundary conditions for open quantum systems driven far from equilibrium, Rev. Mod. Phys. **62**, 745 (1990).

[46] M. V. Fischetti, Master-equation approach to the study of electronic transport in small semiconductor devices, Phys. Rev. B **59**, 4901 (1999).

[47] T. Gonzáles and D. Pardo, Physical models of ohmic contact for Monte Carlo device simulation, Solid-State Electron. **39**, 555 (1996).

[48] W. Kausel, G. Nanz, S. Selberherr, and H. Poetzl, in *Simulation of Semiconductor Devices and Processes*, **3**, Bologna, Sep. 1988, p. 625.

[49] S. E. Laux, Techniques for small-signal analysis of semiconductor devices, IEEE Trans. Electron Devices **ED-32**, 2028 (1985).

[50] S. Kohler, J. Lehmann, and P. Hänggi, Driven quantum transport on the nanoscale, Phys. Rep. **406**, 379 (2005).

[51] J. Charles, P. Sarangapani, R. Golizadeh-Mojarad, R. Andrawis, D. Lemus, X. Guo, D. Mejia, J. E. Fonseca, M. Povolotskyi, T. Kubis, and G. Klimeck, Incoherent transport in NEMO5: realistic and efficient scattering on phonons, J. Comp. Electron. **15**, 1123 (2016).

[52] D. Cimbri, J. Wang, A. Al-Khalidi, and E. Wasige, Resonant tunneling diodes high-speed terahertz wireless communications – a review, IEEE Trans. Terahertz Sci. Technol. **12**, 226 (2022).

[53] J. Wang, M. Naftaly, and E. Wasige, An overview of terahertz imaging with resonant tunneling diodes, MDPI Appl. Sci. **12**, 3822 (2022).

[54] A. Pfenning, S. Krüger, F. Jabeen, L. Worschech, F. Hartmann, and S. Höfling, Single-photon counting with semiconductor resonant tunneling devices, MDPI Nanomater. **12**, 2358 (2022).

[55] J. Chen, J. G. Chen, C. H. Yang, and R. A. Wilson, The $I-V$ characteristics of double barrier resonant tunneling diodes: Observation and calculation on their temperature dependence and asymmetry, J. Appl. Phys. **70**, 3131 (1991).

[56] D. Li, J. Shao, L. Tang, C. Edmunds, G. Gardner, M. J. Manfra, and O. Malis, Temperature-dependence of negative differential resistance in GaN/AlGaN resonant tunneling structures, Semicond. Sci. Technol. **28**, 074024 (2013).

[57] S. Lin, D. Wang, Y. Tong, B. Shen, and X. Wang, III-nitrides based resonant tunneling diodes, J. Phys. D **53**, 253002 (2020).

[58] M. Asada, S. Suzuki, and T. Fukuma, Measurements of temperature characteristics and estimation of terahertz negative differential conductance in resonant-tunneling-diode oscillators, AIP Adv. **7**, 115226 (2017).

[59] R. Lake and S. Datta, Nonequilibrium Green's-function method applied to double-barrier resonant-tunneling diodes, Phys. Rev. B **45**, 6670 (1992).

[60] F. L. Traversa, E. Buccafurri, A. Alarcón, G. Albareda, R. Clerc, F. Calmon, A. Poncet, and X. Oriols, Time-dependent many-particle simulation for resonant tunneling diodes: Interpretation of an analytical small-signal

equivalent circuit, IEEE Trans. Electron Devices **58**, 2104 (2011).

[61] R. Morariu, J. Wang, A. C. Cornescu, A. Al-Khalidi, A. Ofiare, J. M. L. Figueiredo, and E. Wasige, Accurate small-signal equivalent circuit modeling of resonant tunneling diodes to 110 GHz, IEEE Trans. Microwave Theory Tech. **67**, 4332 (2019).

[62] F. Bonani, G. Ghione, M. R. Pinto, and R. K. Smith, An efficient approach to noise analysis through multidimensional physics-based models, IEEE Trans. Electron Devices **45**, 261 (1998).

[63] S. Donati Guerrieri, F. Bonani, F. Bertazzi, and G. Ghione, A unified approach to the sensitivity and variability physics-based modeling of semiconductor devices operated in dynamic conditions. Part I: Large-signal sensitivity, IEEE Trans. Electron Devices **63**, 1195 (2016).

[64] S. Donati Guerrieri, F. Bonani, F. Bertazzi, and G. Ghione, A unified approach to the sensitivity and variability physics-based modeling of semiconductor devices operated in dynamic conditions. Part II: Small-signal and conversion matrix sensitivity, IEEE Trans. Electron Devices **63**, 1202 (2016).